

Ultra-Thin Uncooled Integrable-on-Chip Detector to Measure Wide Infrared Radiation Residue in Lithography Exposure and Metrology Inspection Tools

Jahangiri, Mojtaba; Pawluczyk, Jaroslaw; Dąbrowski, Karol; Nihtianov, Stoyan

DOI

[10.1117/12.2658316](https://doi.org/10.1117/12.2658316)

Publication date

2023

Document Version

Final published version

Citation (APA)

Jahangiri, M., Pawluczyk, J., Dąbrowski, K., & Nihtianov, S. (2023). *Ultra-Thin Uncooled Integrable-on-Chip Detector to Measure Wide Infrared Radiation Residue in Lithography Exposure and Metrology Inspection Tools*. Paper presented at Metrology, Inspection, and Process Control XXXVII 2023, San Jose, United States. <https://doi.org/10.1117/12.2658316>

Important note

To cite this publication, please use the final published version (if applicable). Please check the document version above.

Copyright

Other than for strictly personal use, it is not permitted to download, forward or distribute the text or part of it, without the consent of the author(s) and/or copyright holder(s), unless the work is under an open content license such as Creative Commons.

Takedown policy

Please contact us and provide details if you believe this document breaches copyrights. We will remove access to the work immediately and investigate your claim.

PROCEEDINGS OF SPIE

[SPIDigitalLibrary.org/conference-proceedings-of-spie](https://spiedigitallibrary.org/conference-proceedings-of-spie)

Ultra-thin uncooled integrable-on-chip detector to measure wide infrared radiation residue in lithography exposure and metrology inspection tools

Mojtaba Jahangiri, Jaroslaw Pawluczyk, Karol Dąbrowski, Stoyan Nihtianov

Mojtaba Jahangiri, Jaroslaw Pawluczyk, Karol Dąbrowski, Stoyan Nihtianov, "Ultra-thin uncooled integrable-on-chip detector to measure wide infrared radiation residue in lithography exposure and metrology inspection tools," Proc. SPIE 12496, Metrology, Inspection, and Process Control XXXVII, 1249634 (27 April 2023); doi: 10.1117/12.2658316

SPIE.

Event: SPIE Advanced Lithography + Patterning, 2023, San Jose, California, United States

Ultra-Thin Uncooled Integrable-on-Chip Detector to Measure Wide Infrared Radiation Residue in Lithography Exposure and Metrology Inspection Tools

Mojtaba Jahangiri^{a,*}, Jaroslaw Pawluczyk^{b,c}, Karol Dąbrowski^c, Stoyan Nihtianov^a

^a Department of Microelectronics, Faculty of Electrical Engineering, Mathematics and Computer Science, Delft University of Technology, Mekelweg 4, 2628CD, Delft, Netherlands

^b Institute of Applied Physics, Military University of Technology, 00-908, Warszawa, Poland

^c Vigo Photonics SA, Poznańska 129/133, 05-850 Ożarów Mazowiecki, Poland

ABSTRACT

In modern nano-scale lithography, an essential role of the source, the illumination, and projection lenses is to deliver the precise amount of energy at a specific wavelength to the photoresist deposited on a wafer surface during exposure. Unfortunately, the source of the most advanced lithography processes may produce unwanted infrared components passing through the illumination and projection lenses and reaching the wafer surface. These infrared residues can cause local heating resulting in deformation of the optical elements and the exposed wafer, thus causing deterioration of the image quality. Some infrared spectrum components are in the band from 2 μm to 12 μm . An infrared detector that can measure only these spectral components of the exposure beam, without being affected by the much more powerful exposure spectral component, is helpful for optics diagnostic purposes and improving imaging quality. In this paper, an ultra-thin uncooled integrable-on-chip linear array infrared detector to measure the band of 2-12 μm infrared radiation is designed and fabricated based on the photovoltaic multiple junction heterostructure from VIGO Photonics, made of a HgCdTe narrow bandgap semiconductor. Features such as zero bias, low noise, and fast response, together with a wide active window, make the detector unique for use in the mid-infrared band. Besides lithography applications, the new detector can be useful in testing, inspection, and equipment using infrared sources such as: He-Ne lasers (0.6 to 4 μm), STEAM lasers (2 to 200 μm), CO₂ lasers (5 to 11 μm), InGaAsP lasers (0.8 to 3 μm), and PbSnTe (3 to 20 μm) and PbSnSe (7 to 40 μm) lasers.

Keywords: Infrared detector; Mid-infrared measurement; Photolithography; Metrology;

1. INTRODUCTION

In the semiconductor industry, various light/radiation sources are used for fabrication, inspection, and metrology purposes, ranging from X-ray, EUV (extreme ultraviolet), DUV (deep ultraviolet), visible, and up to near-, mid- and far-infrared. For example, UV bands are primarily used for photolithography [1][2], X-ray bands for material study and nondestructive tests [3][4], visible light for visible surface inspection, and infrared bands for nondestructive inspection [5][6]. The performance of all these systems depends on the accurate control of the light used with respect to spectrum purity and intensity.

Most applications use only one or a few spectral components from a source producing radiation in a wider spectrum [7][8]. The efficiency of the filters that extract only the useful components is essential for the proper operation of the lithography and metrology tools. Unfortunately, due to aging or other factors, spectral components outside the valid spectral range can penetrate into the optical system, deteriorate its performance, and even damage it [9][10]. That is why it is crucial to have the capability to detect the presence of out-of-useful-spectrum components. Fortunately, it is not necessary to scan the complete spectrum for unwanted radiation, as in most cases its band(s) are predictable. One such unwanted band is in the infrared spectrum.

In previous work, we proposed an array of bandpass detectors for measuring spectral components in a wide range, from soft X-ray to near-infrared. The array includes a number of silicon-based detectors with customized characteristics. To each detector is added a narrow-band optical filter for a specific wavelength [11]. Due to its relatively high energy bandgaps, it is not possible to use silicon, or even germanium, for creating detectors for the Medium Wavelength Infrared spectrum (MWIR, 2 to 8 μm) or the Long Wavelength Infrared spectrum (LWIR, 8 to 12 μm) [12]. Only a few narrow

direct bandgap semiconductors, such as InGaAs, InSb, and HgCdTe (MCT), or Sb-based type-two superlattices, can be used for effective detection of such low-energy photons. Furthermore, most of these infrared photon detectors need cryogenic cooling, such as 77K, which makes them bulky and impossible to implement on a chip. Therefore, ultra-thin, uncooled, accurate infrared detectors must be developed and integrated with CMOS chips to reach the aims above [13][14][15][16].

This paper reports a new HgCdTe photodetector with a spectral response from 2 to 12 μm , with acceptable detectivity and noise levels at room temperature, which is an important application advantage. The detector is UV- and visible-light-blind, uncooled (300K), and sensitive to weak IR radiation. Moreover, it is ultra-thin and can be assembled on a silicon substrate. This allows its integration on a silicon die. The detector allows for potential application in portable/small inspection tools for the semiconductor industry. Regarding Wien's law, the peak of black body radiation at room temperature is around 10 μm . As a consequence, this detector can cover heat radiation from around -30°C (12 μm) to 1200°C (2 μm).

With the new detector, we can extend the spectral range covered by the array of bandpass detectors reported in [11] to the MWIR and the LWIR spectrums. By using optical filters with the new detector, specific narrower bands within the IR region can be covered. For example, by adding 1 mm of Sapphire to the detector surface, the spectral window can be limited to 2-6 μm .

Besides lithography applications, the new detector can be useful in testing, inspection, and measurement equipment using infrared sources such as: He-Ne lasers (0.6 to 4 μm), STEAM lasers (2 to 200 μm), CO₂ lasers (5 to 11 μm), InGaAsP lasers (0.8 to 3 μm), and PbSnTe (3 to 20 μm) and PbSnSe (7 to 40 μm) lasers [17].

In summary, several potential applications can benefit from the use of this detector: (1) lithography, (2) positioning systems, (3) microscopy inspection, and (4) infrared single-spectral-component power measurement [18].

Section 2 presents the device fabrication method. In Section 3 the device characterization is reported. Some conclusions are drawn in Section 4.

2. DEVICE FABRICATION METHOD

The device prototype developed has a configuration like those resented in [11]. It is an uncooled 5-pixel linear array chip on a silicon carrier. A critical requirement of the device is an overall thickness of less than 700 μm , as it is to be located among CMOS circuits and connected to them by wire bonding. The individual chip is indium bump flip-chip bonded to the semi-insulating silicon carrier with a thickness of 250 μm . Thus, the device is illuminated through the GaAs substrate, as shown in Figure 1, with an HgCdTe structure at the bottom side of the chip, facing the carrier. The silicon carrier surface is covered by the silicon dioxide insulator, 1 μm thick, on which metal contact pads are deposited to avoid electromagnetic coupling between the metal pads.

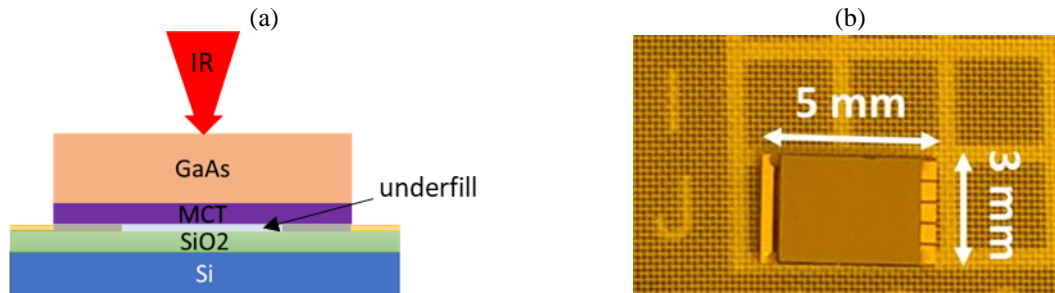


Figure 1. (a) Linear array cross-section, with direction of the infrared (IR) illumination; (b) chip-on-carrier micrograph top view, with a common contact pad on the left and individual pixel output contact pads on the right.

The pixels are 3.2 mm long and 0.5 mm wide, spaced apart by a 0.1 mm gap, as presented in Figure 2. Each pixel is a photodetector with multiple photovoltaic junctions connected in series, which is a proprietary HgCdTe heterostructure manufactured by VIGO Photonics (VIGO), called a PVM in VIGO's catalog. A cross-section of the PVM is shown schematically in Figure 3. The $\langle 111 \rangle$ B-oriented HgCdTe epi-layer with a thickness of a few microns is grown by the Metal Organic Chemical Vapor Deposition process on a GaAs substrate, which is 400 μm thick. Fabrication of the PVM chips involves optical and electrical epi-wafer characterization, photolithography, the etching of mesa structures, ion

milling, contact metallization, and the dicing of wafers into chips. The PVM structure with metallization on HgCdTe is presented in the SEM image in Figure 4. The pixel heterostructure contains 160 photoactive mesa structures (A in Figure 4), distributed periodically within the entire photosensitive area of the pixel. Each mesa is a photovoltaic cell with several heterojunctions, of which those interfacing the radiation absorber layer collect photocarriers and enable the photocurrent flow.

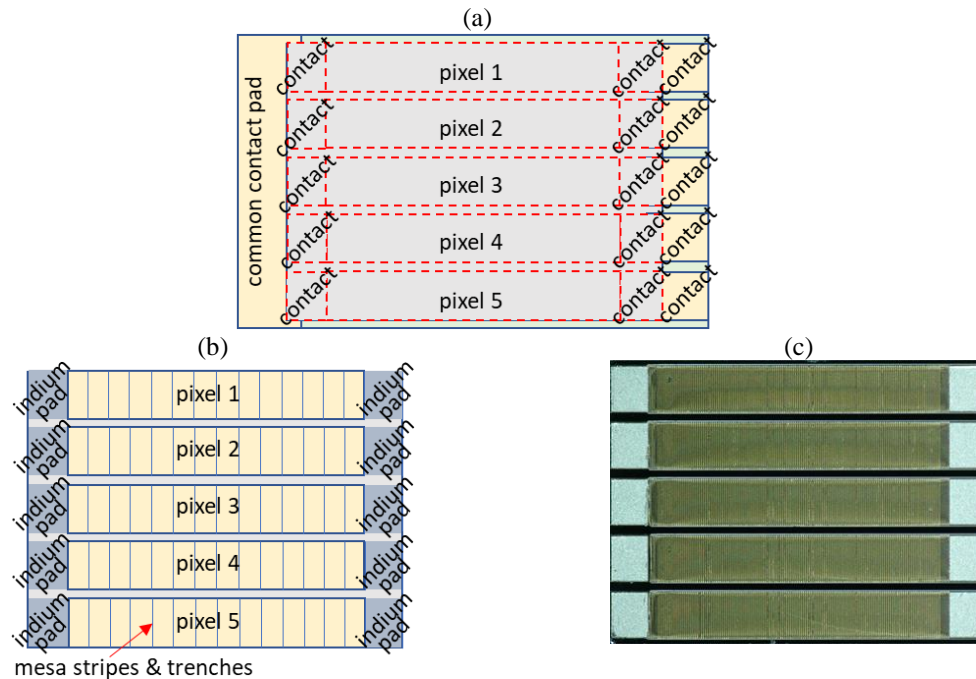


Figure 2. Linear array layout: (a) chip-on-carrier top view with: the delineation of pixels and contact pads, a single pixel area of 3.2 mm x 0.5 mm, pixels separated by a 0.1-mm gap, yellow indicating the gold contact pads on the carrier, contact pads in grey indicating the indium contact pads under chip, a carrier of 5 mm x 3 mm, and a chip of 4 mm x 3 mm; (b) view of the metallized HgCdTe side of the chip, with: the delineation of pixels, indium contact pads, and mesa structures of multiple photovoltaic micro-cells connected in series between indium pads; (c) micrograph of the same metallized side of the chip.

The photocurrent is essentially the diffusion current consisting of electron and hole charge carriers generated by the inter-band absorption of IR, mainly in the absorber narrow-bandgap layer, marked in pink in Figure 3, with light-acceptor (arsenic) doping and p-type conductivity. The composition, doping and thickness of the absorber are optimized with respect to the required radiation spectral range, time constant and magnitude of the photoresponse, and the minimized thermal generation of the carriers. It is interfaced to wide-bandgap areas preventing the thermal generation of carriers, some of which form electrical contacts. The n/n^+ interface, marked in blue in Figure 3, has n-type conductivity; n denotes light donor-doping and n^+ - heavy donor-doping occurring in the vicinity of the surface area defected by ion milling. The latter is used to convert the conduction type from p to n [19]. The P^+ interface, marked in red, is the contact for the holes and is heavily acceptor-doped. An orange layer between P^+ and the metal layer at the mesa top is a narrow bandgap heavily acceptor-doped under-metallization interface, which lowers the metal contact resistance. Each photovoltaic cell, a narrow stripe-shaped mesa with a width of $\sim 10 \mu\text{m}$, is separated from the adjacent cell by an infrared-insensitive trench of similar width (B in Figure 4). The bottom and one side of the trench is covered by a metal path, connecting the adjacent cells in series, i.e. connecting the contact for the holes at the mesa top of the given cell with the contact for the electrons at the mesa side/bottom of the next cell. Although the edges of the photovoltaic cells are not intentionally passivated, they are not short-circuited by the metal path covering one side/edge of each cell/mesa structure because of relatively high metal-contact resistance to the absorber layer at the mesa edge.

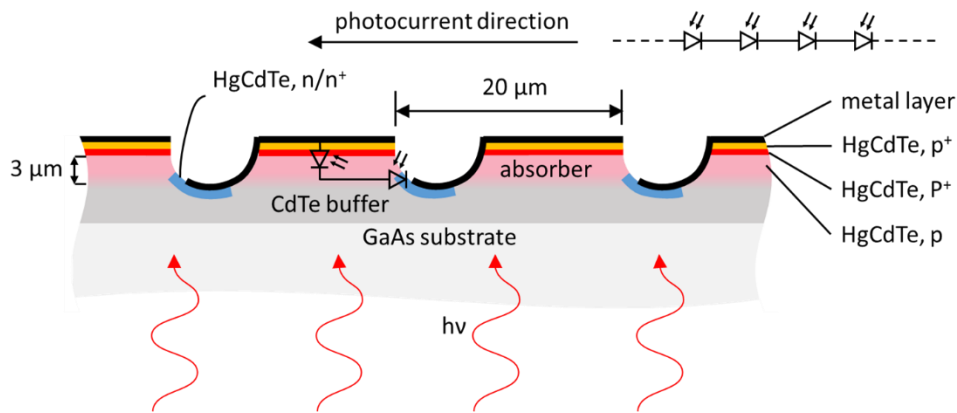


Figure 3. Schematic cross-section in plane perpendicular to the mesa stripes & trenches (Figure 4) of a portion of the PVM periodical structure within a pixel [20]. Symbols of the photodiode on one of the photoactive mesa structures indicate two photoactive heterojunctions interfacing the absorber: the first above the absorber, as the contact for the holes, and the second at the side and bottom of the mesa, as the contact for the electrons.

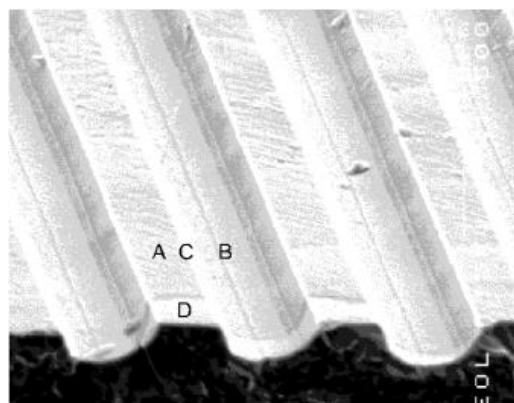


Figure 4. SEM image side view of a PVM periodical structure surface: A - photoactive mesa structure – photovoltaic cell, B - trench, C - non-metalized wall, D - non-metalized region of the device [13][14].

The thickness of the absorber layer is about 3 μm , which is close to the carrier diffusion length but is unfortunately ~ 5 times less than the absorption length of the 10.6 μm radiation, for which this sample of the detector is optimized. Nevertheless, multiple reflections of the 10.6 μm radiation from the side walls of the narrow stripe-shaped mesa with the photovoltaic cell enhance the absorption of the radiation. This is confirmed by a significant red-shift of the long-wavelength spectral cut-off of the PVM in comparison to that of much larger/wider mesa structures made with the same wafer.

Because of the very low resistance-area product (R_0A) of the single photovoltaic cell, equaling only about $5 \times 10^{-5} \text{ ohm} \times \text{cm}^2$ for this spectral range and operation temperature, the connection of multiple photovoltaic cells in series is necessary to obtain a usable detector resistance reaching its optimal value with regard to the output noise of the preamplifier with a detector connected to its input. Such optimal detector resistance for a given operating frequency is close to the ratio of the voltage to current noise spectral density of the preamplifier, related to its input [21]. This ratio is the smallest for preamplifiers with a bi-polar input, for which it typically ranges from ~ 140 to $\sim 500 \text{ ohm}$, and is usually much greater than the input resistance of the transimpedance preamplifiers preferred for photovoltaic detectors, at least at not too high frequencies. For sufficiently high frequencies, above tens of MHz, the above remark should correspond to the respective impedances rather than the resistances. Unfortunately, such low values for the R_0A of a single photovoltaic cell is

comparable to the R0A of a metal contact to HgCdTe and an interface under metallization, therefore the parasitic series resistance of the detector is comparable to its usable resistance and limits the photosignal.

The equivalent electrical circuit of the series connection of multiple photovoltaic cells of the PVM may be represented by the simple small signal lumped-element circuit shown in Figure 5, with the differential parallel R_p and series R_s resistances, and the differential parallel capacitance C_p , as confirmed by measurements.

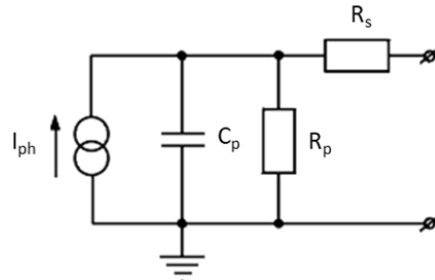


Figure 5. Equivalent small signal circuit of an individual pixel.

3. DEVICE CHARACTERIZATION

The PVM detectors are dedicated for 0 V bias or open output unbiased operation, where photocurrent from thermal background illumination is not present, because the detectors operate at thermal equilibrium with the ambience. Therefore, they exhibit Johnson noise dominance throughout their entire > 100 MHz bandwidth beginning from DC.

The I-V characteristic shape of the pixel is quite a straight line in the ± 2 V bias range, with constant resistance close to 300 ohm – DC measured resistance. The rectifying properties of this series connection of 160 photovoltaic cells within one pixel should be observable only at the reverse bias exceeding the thermal voltage kT/e , equal to 26 mV, per one photovoltaic cell, i.e. at 4.1 V of the total reverse bias, where k is the Boltzmann constant, T is the operating temperature in K, assumed to equal 300 K, and e is the electron charge. A similar resistance is obtained using small signal reflectance measurements with a vector network analyzer [22], performed at frequencies ranging from 1 kHz to beyond the upper corner frequency of the detector. The latter method allows the lumped parameters of the detector equivalent circuit from Figure 5 to be determined. The R_s occurs to be slightly greater than half of the detector resistance, equaling the sum of $R_p + R_s$, while the value of C_p is in the order of a few pF. No significant dependence of the lumped parameters on frequency is observed.

The output voltage is mapped across the photosensitive area of the linear array in the setup shown in Figure 6. The continuous wave (CW) $3 \mu\text{m}$ radiation flux from an inter-band cascade laser is first formed by an optical expander as a parallel beam of the 10 mm diameter and as such shifts across the X Y transverse plane by means of galvo-motor-steered mirrors. Aside from the mirrors, the beam is focused with an aspheric germanium lens of the effective focal length of 50.8 mm on the photosensitive area of the linear array, on a spot of the Gaussian-like distribution of the radiation intensity with the $1/e^2$ diameter of $260 \mu\text{m}$. Although it is a relatively large spot size, thanks to the galvo-mirrors, the rapid scanning allows real-time observations of the linear array scanning result and facilitates fast optical adjustment of the detector position. The photocurrent from the linear array outputs is converted to the voltage signal using 1 MHz transimpedance preamplifiers, one for each pixel output. The voltage signal is then sampled using the acquisition card, from which the samples are sent to a personal computer (PC). The measurement is controlled by a script written in Python programming language, installed on the PC. The script collects and organizes both the sampling data of the output voltages from all five respective preamplifiers, obtained from the acquisition card, and the data of the X Y position of the radiation spot, received from the galvo-motor unit. The galvo-motor action was synchronized by the script with the time the PC receives data from the acquisition card. The script assigns the gathered voltage signal data to the X Y position of the beam spot and presents the results in graphical forms, one of which is presented in Figure 7.

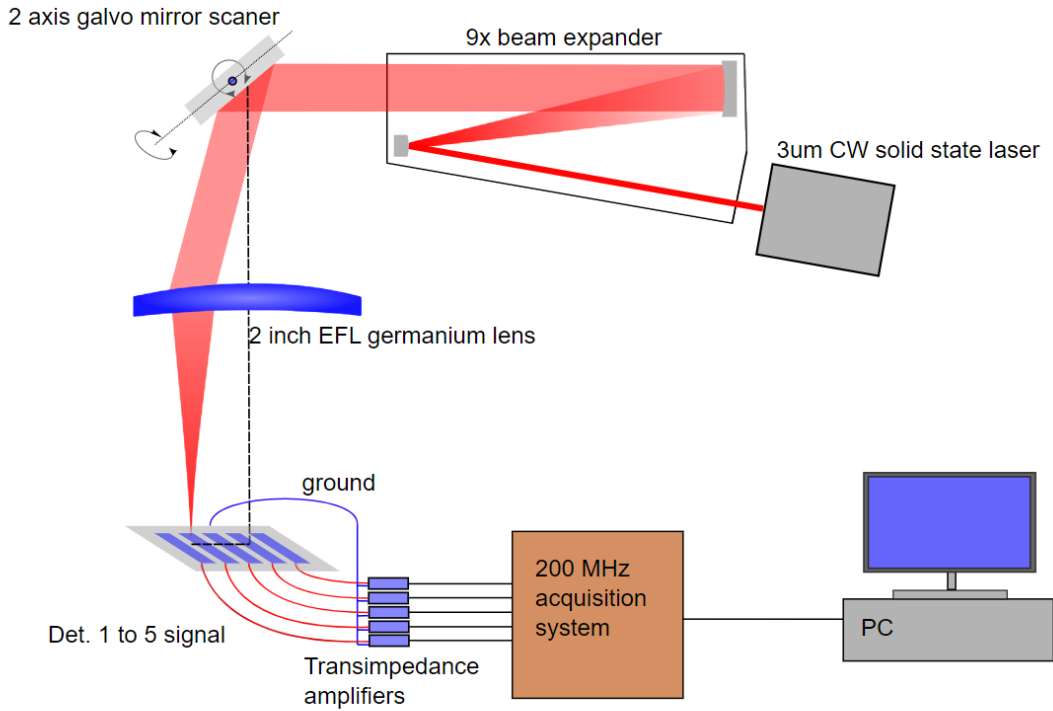


Figure 6. Measurement setup for mapping a photosignal across a linear array.

Figure 8 presents the low frequency spectral characteristics of the pixels. The spectral responsivity is measured with a Fourier transform infrared spectrometer calibrated with a Black Body radiation source with an accuracy of $\pm 20\%$. The short-wavelength cut-off, not visible in this spectral range, equals $0.9 \mu\text{m}$ and results from the GaAs substrate spectral transmission.

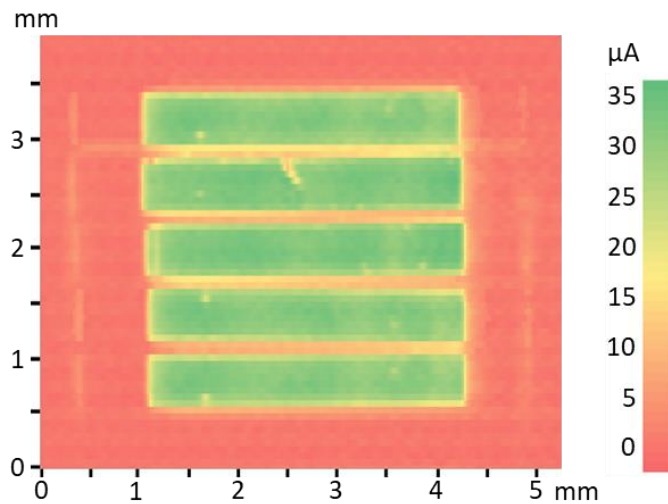


Figure 7. Map of the photosignal, as a result of scanning using the CW 3 μm laser spot of the Gaussian-like radiation distribution with the $1/e^2$ diameter of $260 \mu\text{m}$.

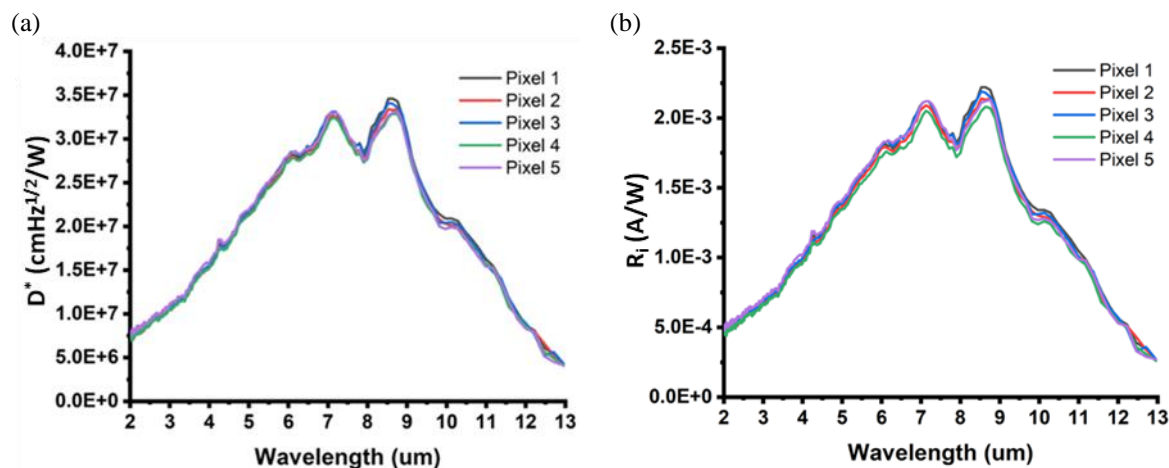


Figure 8. Example spectral characteristics of individual pixels: (a) detectivity, (b) responsivity.

A change in the PVM-10.6 detector responsivity with the polarization of radiation at a wavelength around 10 μm is also observed, of about ±5% or weaker in relation to the responsivity measured at the unpolarized thermal radiation. The responsivity becomes maximal with the polarization perpendicular to the longer sides of the pixel, and minimal with the polarization parallel to them.

4. CONCLUSION

In a nutshell, infrared detectors are undeniable devices for photolithography and metrology inspection tools. Nonetheless, most functional inspection tools use infrared photodetectors with responsivity in the 1 to 2 μm spectral range. The proposed photodetector can extend the inspection range up to 12 μm. This extension brings not only the new capability of measuring unbalanced local temperature in optical components such as lenses, but also early hot spot detection and interior inspection of semiconductors with a bandgap narrower than 0.6 eV. The photodetector introduced is made of a series of HgCdTe photodiodes which are uncooled, and UV/visible-blind. It has a photoresponsivity higher than 5.0E-4 A/W in the 2-12 μm spectral range, with a peak value of >2.0E-3 A/W in the range of 7 to 9 μm. Adding varieties of optical filters can also open opportunities to use the detector for portable micro-spectrometer applications.

REFERENCES

- [1] V. Bakshi, *EUV Lithography*, 2nd ed. SPIE Press, 2018.
- [2] Y. Ozaki and S. Kawata, *Far- and Deep-Ultraviolet Spectroscopy*. Springer Japan, 2015.
- [3] D. K. Bowen and B. K. Tanner, *X-Ray Metrology in Semiconductor Manufacturing*. CRC Press, 2018.
- [4] D. Attwood, A. Sakdinawat, and L. Geniesse, *X-Rays and Extreme Ultraviolet Radiation: Principles and Applications*. Cambridge University Press, 2017.
- [5] K. Takami, "Defect inspection of wafers by laser scattering," *Mater. Sci. Eng. B*, vol. 44, no. 1–3, pp. 181–187, 1997.
- [6] A. C. Rudack, L. W. Kong, and G. G. Baker, "Infrared microscopy for overlay and defect metrology on 3D-interconnect bonded wafers," in *2010 IEEE/SEMI Advanced Semiconductor Manufacturing Conference (ASMC)*, 2010, pp. 347–352, doi: 10.1109/ASMC.2010.5551481.
- [7] A. Tiberj and J. Camassel, "Raman Imaging in Semiconductor Physics: Applications to Microelectronic Materials and Devices BT - Raman Imaging: Techniques and Applications," A. Zoubir, Ed. Berlin, Heidelberg: Springer Berlin Heidelberg, 2012, pp. 39–83.
- [8] R. Juškaitis, N. P. Rea, and T. Wilson, "Semiconductor laser confocal microscopy," *Appl. Opt.*, vol. 33, no. 4, pp. 578–584, 1994, doi: 10.1364/AO.33.000578.

- [9] J. Yang, S. Hwang, Y.-K. An, K. Lee, and H. Sohn, "Multi-spot laser lock-in thermography for real-time imaging of cracks in semiconductor chips during a manufacturing process," *J. Mater. Process. Technol.*, vol. 229, pp. 94–101, 2016, doi: <https://doi.org/10.1016/j.jmatprotec.2015.09.020>.
- [10] J. E. Webb, "Measurement Of Optical Performance Of Photolithographic Lenses," in *Proc.SPIE*, 1984, vol. 0480, pp. 133–140, doi: 10.1117/12.943058.
- [11] M. Jahangiri, P. Sberna, A. Sammak, and S. Nihtianov, "An Array of Bandpass Detectors for Measuring Beam Spectral Components," in *IEEE APSCON 2023*, 2023.
- [12] M. Jahangiri, P. Sberna, A. Sammak, and S. Nihtianov, "Comparative Study of the Resolution of Ge-on-Si Photodetectors for 1 μm Infrared Signals," in *IEEE ONCON 2022*, 2022.
- [13] J. Piotrowski and A. Rogalski, *High-operating-temperature Infrared Photodetectors*. SPIE, 2007.
- [14] P. Capper, J. Garland, S. O. Kasap, and A. Willoughby, *Mercury Cadmium Telluride: Growth, Properties and Applications*. Wiley, 2011.
- [15] A. Piotrowski *et al.*, "MOCVD HgCdTe heterostructures for uncooled infrared photodetectors," in *Quantum Sensing and Nanophotonic Devices II*, 2005, vol. 5732, pp. 273–284.
- [16] W. Gawron *et al.*, "Multiple long wavelength infrared MOCVD grown HgCdTe photodetectors for high temperature conditions," *IEEE Sens. J.*, vol. 21, no. 4, pp. 4509–4516, 2020.
- [17] A. Kozłowska, "Infrared imaging of semiconductor lasers," *Semicond. Sci. Technol.*, vol. 22, no. 8, p. R27, 2007.
- [18] A. Krier, *Mid-infrared Semiconductor Optoelectronics*. Springer London, 2007.
- [19] I. I. Izhnin, K. D. Mynbaev, A. V. Voitsekhovskii, A. G. Korotaev, O. I. Fitsych, and M. Pociask-Bialy, "Ion etching of HgCdTe: Properties, patterns and use as a method for defect studies," *Opto-Electronics Rev.*, vol. 25, no. 2, pp. 148–170, 2017.
- [20] J. Pawluczyk *et al.*, "Higher operation temperature quadrant photon detectors of 2-11 μm wavelength radiation with large photosensitive areas," in *Technologies for Optical Countermeasures XIV*, 2017, vol. 10435, p. 1043505.
- [21] P. Kalinowski, J. Mikołajczyk, A. Piotrowski, and J. Piotrowski, "Recent advances in manufacturing of miniaturized uncooled IR detection modules," *Semicond. Sci. Technol.*, vol. 34, no. 3, p. 33002, 2019.
- [22] M. Żbik, J. Szatkowski, and W. Wiatr, "Time-Domain Characterization of High-Speed Mid-Infrared Photodetectors Using a Laser-Based Non-Linear Vector Network Analyzer System," in *2020 23rd International Microwave and Radar Conference (MIKON)*, 2020, pp. 263–267.